Simulating the radio emissions of dark matter for new high-resolution observations with MeerKAT

M Sarkis and G Beck

School of Physics, University of the Witwatersrand, Private Bag 3, WITS-2050, Johannesburg, South Africa

E-mail: `michael.sarkis@students.wits.ac.za`

Abstract. Recent work has shown that searches for diffuse radio emission by MeerKAT - and eventually the SKA - are well suited to provide some of the strongest constraints yet on dark matter annihilations. To make full use of the observations by these facilities, accurate simulations of the expected dark matter abundance and diffusion mechanisms in these astrophysical objects are required. However, because of the computational costs involved, various mathematical and numerical techniques have been developed to perform the calculations in a feasible manner. Here we provide the first quantitative comparison between methods that are commonly used in the literature, and outline the applicability of each one in various simulation scenarios. These considerations are becoming ever more important as the hunt for dark matter continues into a new era of precision radio observations.

1. Introduction

Despite decades of work, indirect Dark Matter (DM) searches – those that look for the emissions from the annihilation and decay products of DM particles – are yet to find a signal that can be solely attributed to DM. Until such a detection is made, and as our observing capabilities improve with newer and more sophisticated telescopes, we continue to methodically move through the parameter spaces of candidate DM models and eliminate those that conflict with the data. The recent public release of the MeerKAT Galaxy Cluster Legacy Survey data [1], together with recent studies that show the competitiveness of using radio emissions for DM indirect detection [2, 3, 4], provides strong motivation for a renewed and continued effort in radio DM searches. In this work we take a brief but detailed look at the various theoretical aspects involved in the modelling of radio emissions from WIMP DM, and comment on how the choice of model will likely play an important role in indirect DM searches with high-resolution instruments.

Our analysis includes simulations of the DM host environments for two source targets, the Coma galaxy cluster and the M31 galaxy, and a calculation of the synchrotron emissions resulting from WIMP annihilations therein. We model our DM halos with a set of reasonable source parameters and find the emissions after solving the electron propagation equation in each environment. The solution to this equation is one of the major focus points of this work, as the choice of technique used can lead to a non-negligible change in the observed emissions, particularly in smaller source targets where diffusion effects are significant. With < 10 arcsecond resolution capabilities, observations with MeerKAT (and soon the SKA) are for the first time able to probe the inner regions of these targets, which are where the strongest constraints on DM can be found. Therefore, accurate spatial modelling of these targets is essential for us to make full use of the new data.

2. Modelling

The two source targets in this work, the Coma galaxy cluster and the M31 galaxy, were chosen for their well characterised properties in the literature. Of particular importance are the profiles of their magnetic fields and thermal gas densities; as these quantities appear in the modelling process (but are often underspecified) the uncertainty of the final solution depends strongly on the treatment of these factors [5]. However, since the simulation of the halo environment is not the central focus of this work (and for the sake of brevity), we refer the reader to the following sources for details regarding the parameters in the Coma cluster [6, 7] and in the M31 galaxy [8, 9].

In each halo environment, the emission of synchrotron radiation will be determined by the equilibrium distribution (ψ) of charged particles – in this work considered to be electrons and positrons. The evolution of these particles over time is given by the following propagation equation, which includes the dominant effects of energy losses and spatial diffusion:

$$\frac{\partial \psi(\mathbf{x}, E)}{\partial t} = \nabla \cdot (D(\mathbf{x}, E)\nabla\psi(\mathbf{x}, E)) + \frac{\partial}{\partial E}(b(\mathbf{x}, E)\psi(\mathbf{x}, E)) + Q(\mathbf{x}, E). \tag{1}$$

Here D, b and Q are the diffusion, energy-loss and DM annihilation source functions respectively, and the determination of the exact forms of these functions follows the methods laid out in [5].

2.1. Solving the propagation equation

We determine the equilibrium electron distribution ψ using two independent techniques. The first, referred to here as the 'Green's method' [2, 10], uses a Green's function with simplified forms of D and b to calculate Eq. 1 semi-analytically. The second, referred to as the 'ADI method' [11, 12], uses a numerical approach to solve Eq. 1 iteratively. In both methods we consider the halo environment to be spherically symmetric, so that $\mathbf{x} \to r$. As our methodology closely follows the above-mentioned literature, we only summarise these methods and point out any major differences in the following sections.

Green's method If the forms of the diffusion and energy-loss functions are simplified so that they have no spatial dependence, a solution to Eq. 1 can be found directly with the use of Green's functions and image charges. However, these simplifications often have an impact on the calculated emissions (for a review on this topic, see [5]). In this work we use non-weighted averages for the magnetic field and thermal gas densities, found using an averaging scale radius that matches the scale radius of the DM halo. This choice encapsulates the region in the halo that contains the majority of WIMP annihilations – and thus best represents the spatial structure of the halo – while allowing us to forgo any explicit spatial dependence in Eq. 1. Now, the equilibrium distribution of electrons in the halo can be calculated using

$$\psi(r, E) = \frac{1}{b(E)} \int_E^{m_\chi} \mathrm{d}E' G(r, \Delta v)Q(r, E'), \tag{2}$$

with m_χ as the WIMP mass and the Green's function (G) given by

$$G(r, \Delta v) = \frac{1}{\sqrt{4\pi\Delta v}} \sum_{n=-\infty}^{\infty} (-1)^n \int_0^{r_{\max}} \mathrm{d}r' \frac{r'}{r_n} \left(\mathrm{e}^{-\frac{(r'-r_n)^2}{4\Delta v}} - \mathrm{e}^{-\frac{(r'+r_n)^2}{4\Delta v}} \right) \frac{Q(r')}{Q(r)}. \tag{3}$$

Here $r_{\max}$ is the maximum radius for any diffusion processes and $r_n = (-1)^n r + 2nr_{\max}$ are the image charge locations. The quantity Δv is calculated as

$$\Delta v = v(u(E)) - v(u(E')), \tag{4}$$

where

$$v(u(E)) = \int_{u_{\min}}^{u(E)} \mathrm{d}x D(x) \qquad \text{and} \qquad u(E) = \int_E^{E_{\max}} \frac{\mathrm{d}x}{b(x)}. \tag{5}$$

ADI method In this method, we discretise Eq. 1 and solve for the equilibrium distribution iteratively. Since we now keep the spatial (radial) dependence in the diffusion and energy loss functions, the problem becomes 2-dimensional in energy and space. Using a traditional finite-difference technique in this scenario could be computationally expensive, which is why we opt for a method that uses so-called 'operator splitting' to treat each dimension separately and divide the problem into smaller, more manageable pieces. Thus, during each step of the method we use a general form of the 1-dimensional Crank-Nicolson (CN) scheme (see, for instance, [13]) which is a finite-differencing technique that includes the average of second-order implicit and explicit terms in the updating equation, leveraging the unconditional stability of a fully implicit method while maintaining second-order accuracy in space and time. This scheme is relatively easy to solve, as the updating equation turns out to be a set of linear equations with tridiagonal coefficient matrices. We write this, as in [11, 12], as

$$-\frac{\alpha_1}{2}\psi_{x-1}^{n+1} + \left(1 + \frac{\alpha_2}{2}\right)\psi_x^{n+1} - \frac{\alpha_3}{2}\psi_{x+1}^{n+1} = \frac{\alpha_1}{2}\psi_{x-1}^n + \left(1 - \frac{\alpha_2}{2}\right)\psi_x^n + \frac{\alpha_3}{2}\psi_{x+1}^n + Q_x\Delta t. \quad (6)$$

Here the factors of the diffusion and energy loss functions have been included generally in the coefficients α, n is the temporal grid index (with the spacing between indices given by Δt) and x represents either the energy or spatial grid index. Before the correct forms of the α coefficients are calculated, we make the variable transformations $\tilde{r} = \log_{10}(r/r_0)$ and $\tilde{E} = \log_{10}(E/E_0)$ (similarly to [12], except with base 10 instead of e). These variables allow us to more accurately track the electron distribution in our grids when the involved processes operate over a wide range of physical scales. The diffusion and energy loss operators are then discretised as follows:

$$\frac{1}{r^2}\frac{\partial}{\partial r}\left(r^2 D\frac{\partial \psi}{\partial r}\right) \to C_{\tilde{r}}^{-2}\left[\frac{\psi_{i+1} - \psi_{i-1}}{2\Delta\tilde{r}}\left(\log(10)D + \frac{\partial D}{\partial \tilde{r}}\right)\bigg|_{\tilde{r}_i} + \frac{\psi_{i+1} - 2\psi_i + \psi_{i-1}}{\Delta\tilde{r}^2}D|_{\tilde{r}_i}\right] \quad (7)$$

for radius and

$$\frac{\partial}{\partial E}(b\psi) \to C_{\tilde{E}}^{-1}\left[\frac{b\psi_{j+1} - b\psi_j}{\Delta\tilde{E}}\right]_{\tilde{E}_j} \quad (8)$$

for energy, where $C_{\tilde{r}} = (r_0\log(10)10^{\tilde{r}_i})$, $C_{\tilde{E}} = (E_0\log(10)10^{\tilde{E}_j})$ and $\Delta\tilde{r}$, $\Delta\tilde{E}$ represent the radial and energy grid spacings, respectively. We use i and j to denote positions in the radial and energy grids, and have omitted the temporal indices as these forms will apply to both implicit and explicit terms in the same way. Also note that in the case of energy losses, we only consider upstream differencing. The α values can now be found by taking Eqs. 7 and 8 and equating coefficients with Eq. 6; once these are found the updating equation can be solved with some matrix solution algorithm. If we represent the discretisation schemes shown above by the symbol Ψ, the overall iterative solution can be summarised with the steps

$$\psi^{n+1/2} = \Psi_{\tilde{E}}(\psi^n)$$
$$\psi^{n+1} = \Psi_{\tilde{r}}(\psi^{n+1/2}), \quad (9)$$

which are repeatedly solved (using Eq. 6) until the value of ψ has converged to the equilibrium value. The other minutiae of this method, including initial and boundary conditions, convergence criteria and stability considerations, can be found in [11, 12].

2.2. Synchrotron emissions
Once found via the Green's or ADI methods, the equilibrium distribution is used to calculate the radio emissivity, given by

$$j_{\text{sync}}(\nu, r) = \int_0^{M_\chi} dE\, \psi_{e^\pm}(E, r)P_{\text{sync}}(\nu, E, r), \quad (10)$$

where ν is the synchrotron frequency, $\psi_{e\pm}$ is the sum of electron and positron equilibrium distributions and P_{sync} is the power emitted by an electron with an energy of E (this is calculated as in [2]). The emissivity is then used to calculate the two main results in this work; firstly the surface brightness curves,

$$I_{\text{sync}}(\nu, R) = \int dl \, \frac{j_{\text{sync}}(\nu, \sqrt{R^2 + l^2})}{4\pi} \, , \tag{11}$$

where l is the line-of-sight to a point in the halo at radius R, and secondly the integrated flux density,

$$S_{\text{sync}}(\nu, R) = \int_0^R d^3 r' \, \frac{j_{\text{sync}}(\nu, r')}{4\pi(d_L^2 + (r')^2)} \, , \tag{12}$$

where the emissivity is integrated over the region enclosed by R and d_L is the luminosity distance to the target.

3. Results

Here we provide the details of the simulations we have performed, and show the results for two observables - the radio surface brightness (Eq. 11) and integrated flux (Eq. 12). We use a set of reasonable source parameters for the halo environment that respect observational constraints, and aim to use WIMP parameter values that are representative of the many viable candidates. We thus consider a large range of particle masses, from 10 to 1000 GeV, and use a set of four annihilation channels, $\{b\bar{b}, e^+e^-, \mu^+\mu^-, \tau^+\tau^-\}$.
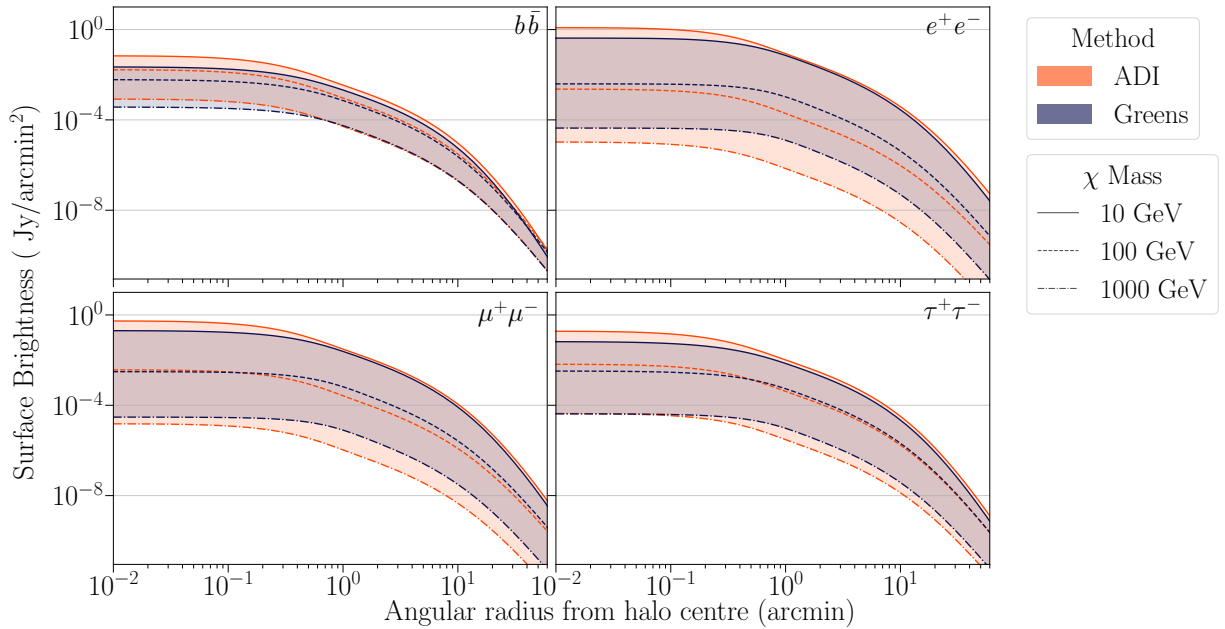

Figure 1. Surface brightness curves for the Coma galaxy cluster. Each of the four panels show different annihilation channels, given by the label in the top right of each plot. The two methods are represented by the two colours, and the shaded region represents the WIMP mass range between the minimum (10 GeV) and maximum (1000 GeV). In these results we set $\nu = 0.5$ GHz.

These results do not comprehensively cover the available parameter spaces; the focus here is on a comparison between the two solution methods, particularly in the way that they differ with
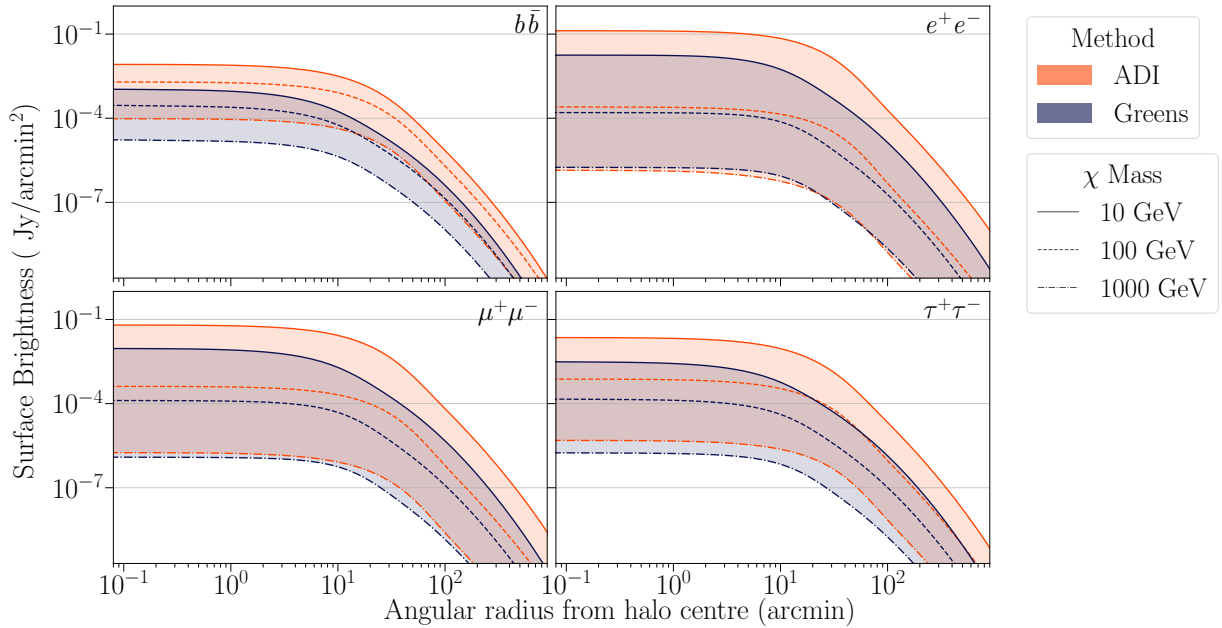
Figure 2. Surface brightness curves for the M31 galaxy. Plot details follow those in Figure 1.
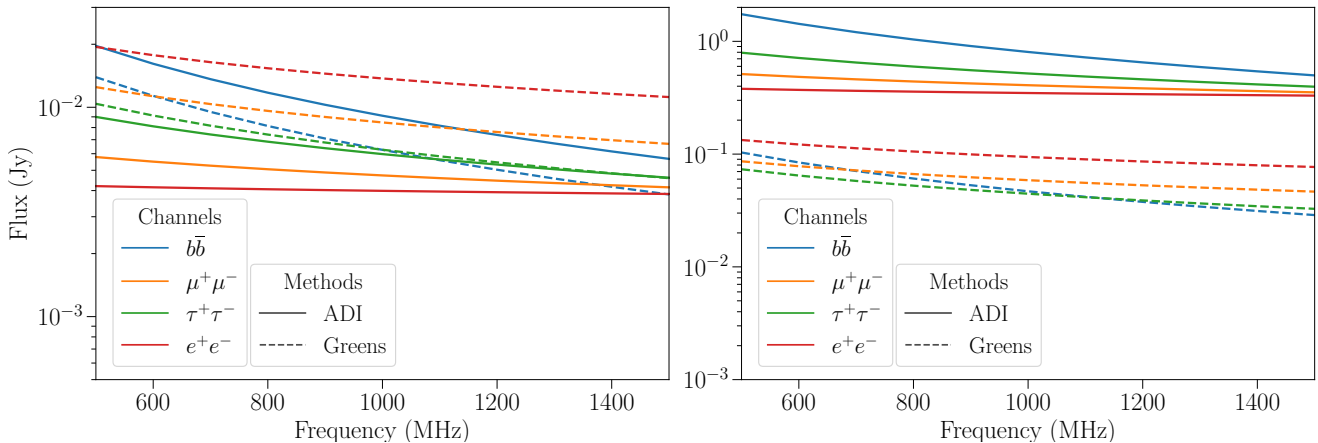
Figure 3. The integrated fluxes, calculated using Eq. 12, for the Coma galaxy cluster (left) and the M31 galaxy (right). The different linestyles represent the two solution methods presented in Sec. 2.1, and each colour indicates the use of a different annihilation channel.

various source targets. Therefore, we show the results for each method side-by-side, and in the same manner for both of our source targets. In Figs. 1 and 2 we show the surface brightness curves for the Coma cluster and M33 respectively, and Fig. 3 shows the integrated flux from these targets in the left- and right-hand panels, for a range of frequencies. The flux in these cases are calculated over the entire halo, *i.e.* from the centre up to the virial radius.

4. Discussion and conclusions

In Figs. 1 and 2, we see generally good agreement between the Green's and ADI methods, which provides evidence for consistency between the methods. Noticeably however, we see more variation between the methods in the M31 galaxy than we do for the Coma galaxy cluster. Our explanation for this lies in the mathematical techniques employed by each method, and how

they each treat the spatial dependence of the diffusion function in particular. In the galaxy cluster environment of Coma, diffusion effects are negligible on sufficiently large scales [10, 5], whereas in the physically smaller galaxy, diffusion effects start to influence the surface brightness distribution at all relevant scales. Since the Green's and ADI methods use a spatially independent and dependent diffusion function (respectively), the resulting equilibrium distribution from these two methods begins to differ in the environments where the scales in question do not greatly exceed the diffusion length. This trend is also seen in the fluxes from Fig. 3, which show a clear variance in all channels for the M31 galaxy, and relative agreement for all channels in the Coma cluster. Based on these results and the comparison of target environments presented in [5], we also expect that smaller target environments (like the dwarf spheroidal satellite galaxies of the Milky Way) would show further variance between the solution methods, as diffusion effects would be even more significant in these environments.

The other notable result we see from these simulations is that the methods differ on small scales, even in the large Coma cluster. This is significant, as the inner regions of the DM halos are where we would observe the strongest emissions. With high-resolution radio interferometers allowing us to resolve these smaller scales, our models could be tested against the strongest possible DM emissions, allowing us to find the most stringent constraints on DM properties. In this regard, the surface brightness curves displayed here would be especially valuable results when determining new observational limits, as their emission profiles are highly dependent on the spatial structure of the DM halo.

With the impressive spatial resolution of telescopes like MeerKAT and the SKA, we are now able to probe the inner regions of these DM halos – regions which have formerly been hidden from our view. The need for accurate modelling techniques is thus more necessary than ever before, and the considerations presented in this work should help inform the modelling choices made in future radio searches for DM.

References
[1] Knowles K, Cotton W D, Rudnick L *et al.* 2022 *Astronomy & Astrophysics* **657** A56
[2] Beck G 2019 *Galaxies* **7** 16
[3] Regis M, Reynoso-Cordova J, Filipović M D *et al.* 2021 *Journal of Cosmology and Astroparticle Physics* **2021** 046
[4] Chan M 2021 *Galaxies* **9** 11
[5] Sarkis M and Beck G 2022 *The Proceedings of SAIP2021* ed Prinsloo A (UJ) pp 316–322 ISBN 978-0-620-97693-0
[6] Bonafede A, Feretti L, Murgia M *et al.* 2010 *Astronomy and Astrophysics* **513** A30
[7] Łokas E L and Mamon G A 2003 *Monthly Notices of the Royal Astronomical Society* **343** 401–412
[8] Ruiz-Granados B, Rubiño-Martín J A, Florido E *et al.* 2010 *The Astrophysical Journal* **723** L44–L48
[9] Tamm A, Tempel E, Tenjes P *et al.* 2012 *Astronomy & Astrophysics* **546** A4
[10] Colafrancesco S, Profumo S and Ullio P 2006 *Astronomy & Astrophysics* **455** 21–43
[11] Strong A W and Moskalenko I V 1998 *The Astrophysical Journal* **509** 212–228
[12] Regis M, Richter L, Colafrancesco S *et al.* 2015 *Monthly Notices of the Royal Astronomical Society* **448** 3747–3765
[13] Press W H, Teukolsky S A and Vetterling W T 2007 *Numerical Recipes: The Art of Scientific Computing* 3rd ed (Cambridge University Press) ISBN 978-0-521-88068-8